



Urchin-like hierarchical CoZnAl-LDH/RGO/g-C₃N₄ hybrid as a Z-scheme photocatalyst for efficient and selective CO₂ reduction



Yong Yang^{a,b,*¹}, Jiajia Wu^{a,1}, Tingting Xiao^a, Zheng Tang^a, Jinyou Shen^{a,*}, Haijin Li^b, Yong Zhou^b, Zhigang Zou^b

^a Key Laboratory of Soft Chemistry and Functional Materials, Ministry of Education, Nanjing University of Science and Technology, Nanjing 210094, PR China

^b Eco-Materials and Renewable Energy Research Centre (ERERC), Jiangsu Key Laboratory for Nano Technology, School of Physics, Nanjing University, Nanjing 210093, PR China

ARTICLE INFO

Keywords:

Urchin-like
Layered double hydroxides
Photocatalysis
CO₂ reduction
Z-scheme

ABSTRACT

A unique urchin-like CoZnAl-LDH/RGO/g-C₃N₄ (LDH/RGO/CN) Z-scheme photocatalyst, which is fabricated by the hydrothermal synthesis of CoZnAl-LDH and the *in situ* loading of RGO and g-C₃N₄, is developed for the photocatalytic conversion of CO₂. The special spiny external surface and hollow inner cavity endow LDH/RGO/CN with a significantly enhanced light-harvesting capacity. The well-distributed g-C₃N₄ nanosheets on the CoZnAl-LDH nanoplates, combined with RGO as an electron mediator, constructs an excellent heterosystem with numerous interfaces, efficient charge separation and highly exposed catalytic active sites. The Z-scheme charge-transfer process promotes the oxidizability and reducibility of CoZnAl-LDH and g-C₃N₄. Furthermore, the synergistic effect among the components contributes to intense adsorption and chemical activation towards CO₂, which reduces the reaction barrier for CO₂ photoreduction. As a result, the optimized LDH/RGO/CN exhibits highly efficient and selective photocatalytic CO₂ conversion to CO. The special 3D urchin-like architecture paves a new way for design of photocatalyst with ideal performance.

1. Introduction

With the industrialization and modernization of human society, consumption of fossil fuels has rapidly increased. The burning of these fossil fuels leads to a continuous emission of greenhouse gases, which results in a serious global warming issue [1–3]. Among various greenhouse gases, CO₂ has been respected as the major concern. The increase of the atmospheric CO₂ concentration poses a huge threat to the ecological balance of the earth and the survival of human beings, therefore, the effective reduction and reasonable utilization of CO₂ have become an important topic. Compared with the capture and reuse means, photocatalytic CO₂ reduction has turned out to be a favourable alternative that can utilize inexhaustible solar energy to convert greenhouse gas into hydrocarbon fuels. The challenges caused by environmental issues and the energy crisis may be overcome by this economical strategy, as they provide an advisable way to “kill two birds with one stone” [4–7].

During the past few decades, great endeavours have been made to develop a highly efficient photocatalytic system for CO₂ reduction, and

notable progress has been achieved. Metal oxides are the most studied photocatalysts for CO₂ conversion, such as TiO₂ [8,9], ZnO [10,11], WO₃ [12,13], Zn₂GeO₄ [14], Bi₂WO₆ [15,16], Fe₂V₄O₁₃ [17], and layered double hydroxides (LDHs) [18,19], et al. Among them, LDHs are a class of layered composite metal hydroxides that consist of divalent and trivalent metal cations plain with exchangeable anions between the layers [20,21]. The anions and metal cations of LDHs can be exchanged easily, allowing for great flexibility in the electronic structure of these materials. Moreover, owing to the alkalinity and intense adsorption capacity, LDHs attract great attention in the field of photocatalytic CO₂ reduction. Izumi et al. first reported LDHs as the photocatalyst for CO₂ reduction [22]. The divalent Cu²⁺, Zn²⁺ and trivalent Al³⁺, Ga³⁺ were used as plate cations. Zn-Al LDH showed the best photocatalytic activity due to its excellent CO₂ adsorption capacity. Tanaka's group delicately investigated the photocatalytic conversion of CO₂ in water over Mg-In LDH, and they attributed the superiority of this system to the surface base site belonging to LDHs [23]. Iguchi et al. used AlF₆³⁻ for the fluorination of Mg-Al LDH and Ni-Al LDH, and the selectivity and yield for CO were both improved in the presence of Cl⁻

* Corresponding author at: Key Laboratory of Soft Chemistry and Functional Materials, Ministry of Education, Nanjing University of Science and Technology, Nanjing 210094, PR China.

E-mail addresses: yychem@njjust.edu.cn (Y. Yang), shenjinyou@mail.njust.edu.cn (J. Shen).

¹ These two authors contributed equally to this work.

and irradiation of UV light [24]. Although native LDHs have exhibited great potential for photocatalytic CO₂ reduction, the drawbacks, such as the recombination of photoinduced charge carriers, insufficient light harvesting property and weak reduction capacity, still limit the conversion efficiency.

To enhance the charge separation of photocatalysts, an effective approach is to build an elaborate semiconductor heterojunction. However, LDHs are usually used as the adsorbent for CO₂ in most of the composite photocatalytic systems [25,26]. LDHs-based heterojunctions are seldomly reported for photocatalytic CO₂ conversions. Kumar et al. used P25 nanoparticles to modify CoAl-LDH, and the hierarchical P25@CoAl-LDH composites exhibited good activity and selectivity for aqueous CO₂ photoreduction, owing to the enhanced separation efficiency of photoinduced charge carriers with the mechanism of a type-II heterojunction [27]. Recently, the g-C₃N₄/NiAl-LDH hybrid was developed for photocatalytic CO₂ reduction, the CO evolution rate was 8.2 μmol g⁻¹ h⁻¹, and the selectivity towards CO reached almost 82%. The charge transport also obeyed the type-II mode [28]. Our group has reported a crystal facet-based homojunction that was derived from ZnSn(OH)₆, the well-controlled exposure of {100} and {111} facets facilitated the spatial separation of charge carriers, and the yield of the product upon photoreduction of CO₂ was thus improved [29]. Based on the heterostructures, effective separation of the charge carriers was realized, and the photocatalytic performance and stability of photocatalysts was improved. Unfortunately, a Z-scheme heterojunction that is based on LDHs for photocatalytic CO₂ conversion, which most resembles the natural photosynthesis system, has rarely been reported.

As a typical organic semiconductor with a two-dimensional layered structure, graphitic carbon nitride (g-C₃N₄) has been widely investigated in the field of solar water splitting and environmental remediation [30–35]. An appropriate band structure, facile preparation, peculiar physicochemical stability and “earth-abundant” features have made g-C₃N₄ one of the most potential and attractive photocatalysts [36–39]. Owing to the construction by nitrogen-rich π-conjugated hydrocarbons and favourable reduction potential, g-C₃N₄ is also reasonably expected to present superior capacity for photocatalytic CO₂ conversion. However, the actual performance for g-C₃N₄ is unsatisfactory, and much effort has to be made for improving the separation efficiency of photoinduced charge carriers. Therefore, designing Z-scheme heterostructures that are compatible with g-C₃N₄ for a highly efficient photocatalytic reduction of CO₂ is urgently desirable.

As a typical organic semiconductor with two-dimensional layered structure, graphitic carbon nitride (g-C₃N₄) has been widely investigated in the field of solar water splitting and environmental remediation [30–35]. The appropriate band structure, facile preparation, peculiar physicochemical stability and “earth-abundant” features have made g-C₃N₄ become one of the most potential and attractive photocatalyst [36–39]. Owing to the constructing by nitrogen-riched π-conjugated hydrocarbons and favorable reduction potential, g-C₃N₄ is also reasonably expected to present superior capacity for photocatalytic CO₂ conversion. However, the actual performance for g-C₃N₄ is unsatisfied, and much effort has to be made for improving the separation efficiency of photoinduced charge carriers. Therefore, designing of Z-scheme heterostructures compatible with g-C₃N₄ for highly efficient photocatalytic reduction of CO₂ is urgently desirable.

Herein, an urchin-like CoZnAl-LDH/RGO/g-C₃N₄ photocatalyst with the mode of a Z-scheme charge flow was constructed. This special hierarchical architecture with a hollow inner cavity and spiny external surface endows the hybrid with a high specific surface area, favourable efficiency of mass transfer and enhanced capacity for light-harvesting and the utilization of photons. In addition to boosting the separation of light-induced charge carriers, the oxidizability and reducibility that belong to CoZnAl-LDH and g-C₃N₄ are efficiently promoted, which have synchronously been verified by an active species trapping experiment and an electron spin resonance (ESR) investigation. The effective adsorption and chemical activation of CO₂ on the CoZnAl-LDH/RGO/g-

C₃N₄ hybrid decrease the energy barrier for photocatalytic reduction. As a result, the CO formation rate on the urchin-like CoZnAl-LDH/RGO/g-C₃N₄ was efficiently enhanced compared with the corresponding counterparts. To the best of our knowledge, it is the first LDH-based Z-scheme heterojunction towards photocatalytic CO₂ reduction. The special 3D hierarchical architecture provides new strategy and opportunity for design of photocatalyst for efficient photocatalytic CO₂ conversion.

2. Experimental

2.1. Chemicals and materials

Co(NO₃)₂·6H₂O (99%), Zn(NO₃)₂·6H₂O (99%), Al(NO₃)₃·9H₂O (99%) were all obtained from Aladdin and used as the precursors for CoZnAl-LDH. Melamine (Aladdin, 99%) was used as a precursor for preparation of g-C₃N₄. Graphite powder (98%) and sodium borohydride (98%) were supplied by Aladdin. 5, 5-dimethyl-1-pyrroline-N-oxide (DMPO) purchased from Sigma-Aldrich was used as the trapping agent for investigation of ·OH and ·O₂[−] radicals. Urea was the product of Chengdu Kelong Chemical Reagent Factory, and other chemicals used in the experiments were purchased from the Shanghai Chemical Reagent Company.

2.2. Photocatalysts preparation

2.2.1. Preparation of g-C₃N₄ and RGO

g-C₃N₄ was synthesized by heating melamine in air at 550 °C for 4 h. RGO was prepared according to a modified Hummers' method [40]. 1.0 g graphite powder and 0.5 g sodium nitrate (NaNO₃) were added to 24 mL of concentrated sulfuric acid (H₂SO₄, 98%) in an ice-bath, and the mixture was stirred for 30 min. 3.0 g potassium permanganate (KMnO₄) was then added to form a brown paste at room temperature. 30 mL deionized water was slowly added into the above paste and stirred for 24 h. Finally, 3.5 mL hydrogen dioxide (H₂O₂, 30 wt%) was dropped for completing the oxidation process. The precipitation was washed with HCl (5 wt%) several times and dried at 80 °C for 12 h to obtain graphene oxide (GO). Subsequently, 0.1 g GO was dispersed in 100 mL of deionized water by sonication for 30 min, then 1.0 g sodium borohydride (NaBH₄) was added. RGO nanosheet was obtained by refluxing the suspension for 8 h.

2.2.2. Preparation of CoZnAl-LDH/RGO/g-C₃N₄ hybrid

Fig. 1a illustrates the *in-situ* loading of g-C₃N₄ and RGO on CoZnAl-LDH. 10 mg RGO and different amounts of g-C₃N₄ were dispersed in 30 mL of deionized water and ultrasonicated for 30 min. Co(NO₃)₂·6H₂O (0.1456 g), Zn(NO₃)₂·6H₂O (0.1487 g) and Al(NO₃)₃·9H₂O (0.1876 g) were dissolved in 20 mL of deionized water. Meanwhile, 20 mL urea solution (1.0 M) was added. The solution was then dropped into the above-mentioned suspension under vigorous stirring. Then, the mixture was transferred into a Teflon-lined autoclave (100 mL) and kept at 180 °C for 6 h. During the crystallization process, g-C₃N₄ and RGO were deposited on the skeleton of CoZnAl-LDH. The obtained precipitation was centrifuged and washed repeatedly with deionized water and alcohol. In this manner, CoZnAl-LDH/RGO/g-C₃N₄ composites with different weight ratios of g-C₃N₄ (0.05 g, 0.1 g and 0.15 g) were obtained and denoted as LDH/RGO/CN-1, LDH/RGO/CN-2 and LDH/RGO/CN-3. For comparison, CoZnAl-LDH/g-C₃N₄ (LDH/CN) without RGO and the bare CoZnAl-LDH were also prepared with the same procedure.

2.3. Catalyst characterization

X-ray diffraction (XRD) measurements were performed on a Brucker D8 diffractometer with Cu Kα radiation source. Fourier transform infrared (FTIR) spectra were recorded on a Nicolet Nexus-870 infrared

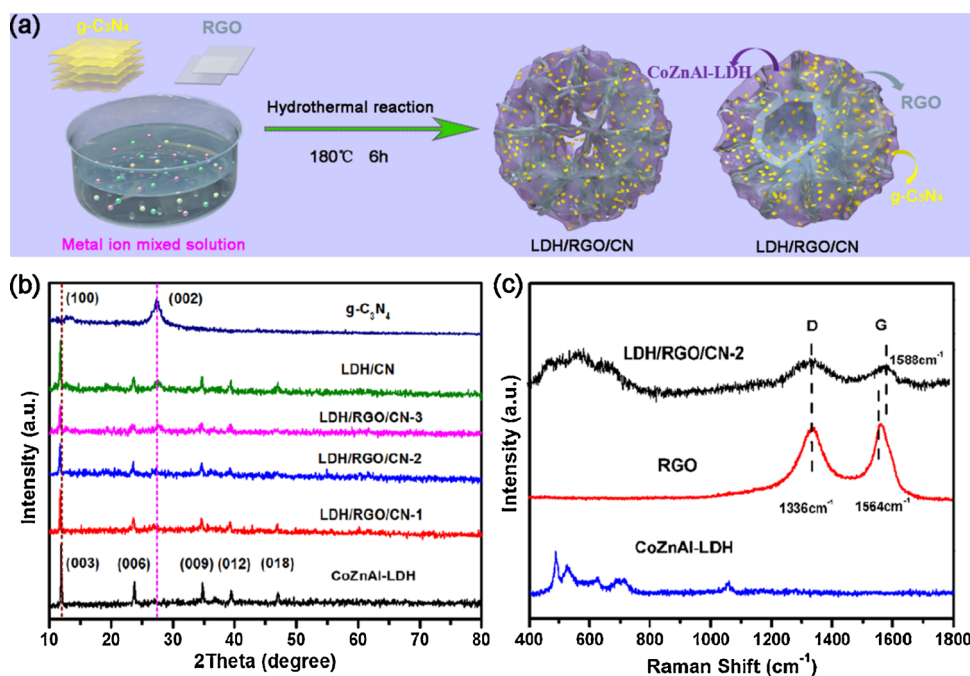


Fig. 1. (a) Illustration for the synthesis of urchin-like CoZnAl-LDH/RGO/g-C₃N₄ hybrid; (b) XRD patterns of the as-prepared samples and (c) Raman spectra of CoZnAl-LDH, RGO and LDH/RGO/CN-2.

spectrometer. Morphologies of the samples were observed by field-emission scanning electron microscopy (FESEM, HITACHI S-4800) equipped with an energy-dispersive X-ray spectroscopy (EDS, Oxford instruments X-Max). Transmission electron microscopy (TEM) images were recorded by a FEI Tecnai F20 microscope at an accelerating voltage of 100 kV. Thermogravimetric analysis (TGA) was performed on a TGA/SDTA851E instrument under N₂ atmosphere. Zeta potential measurement was performed on Zetasizer Nano ZS90 (Malvern). X-ray photoelectron spectroscopy (XPS) was carried out on an RBD upgraded PHI-5000C ESCA system (Perkin-Elmer) with Mg K α radiation ($\hbar\omega = 1253.6$ eV). The binding energy of C1s (284.6 eV) was used to calibrate the binding energies. The specific surface areas and pore diameter distributions were measured by nitrogen adsorption-desorption isotherm at 77 K by an automatic surface area analyzer (Micromeritics TriStar-3000, USA), the samples were dehydrated in advance at 423 K for 3 h in the flowing N₂. UV-vis diffuse reflectance spectrum (UV-vis-DRS) was measured on a Shimadzu UV-2600 spectrometer and transformed into absorption spectrum with Kubelka-Munk relationship. *In-situ* DRIFTS for CO₂ adsorption was measured on the reconstructive FT-IR-6300 spectrometer (Shimadzu Co., Japan) equipped with a liquid N₂ cooled MCT detector. Photoluminescence (PL) emission spectra were recorded on a PerkinElmer LS 55 Fluorescence spectrometer at 355 nm. The photoluminescence (PL) decay profiles were obtained on a Horiba Jobin-Yvon Fluorolog-3-21-TCSPEC spectrometer. The electron spin resonance (ESR) investigations were conducted on a Bruker EMX-10/12 ESR spectrometer.

2.4. Evaluation of photocatalytic activity

For the photocatalytic reduction of CO₂, 50 mg of sample was uniformly dispersed on the glass reactor with an area of 4.2 cm². A 300 W Xenon arc lamp was used as the light source of photocatalytic reaction. The volume of reaction system was about 420 mL. Before the irradiation, the system was vacuum-treated several times, and then the high purity of CO₂ gas was introduced into the reaction setup for reaching ambient pressure. 0.4 mL of deionized water was injected into the reaction system as sacrificial agent. The as-prepared photocatalysts were allowed to equilibrate in the CO₂/H₂O atmosphere for several hours to

ensure that the adsorption of gas molecules was complete. During the irradiation, about 1 mL of gas was continually taken from the reaction cell at given time intervals for subsequent analysis by using a gas chromatography (GC-2014C, Shimadzu Corp., Japan), which was equipped with both FID and TCD detectors. A MS-13X and two PN packed columns were used for separating the products. The carrier gas was high-purity argon gas. The isotope-labelled experiment was performed using ¹³CO₂ instead of ¹²CO₂, and the products were analysed using gas chromatography-mass spectrometry (7890A and 5975C, Agilent). The apparent quantum yield (AQY) for CO production was evaluated in a similar process except that a 385 nm LED (5 W, Beijing Perfectlight Technology Co. Ltd., China) was employed as the light source. The AQY was estimated by formula of

$$\text{AQE (\%)} = \frac{N_{\text{electron}}}{N_{\text{photon}}} = \frac{2 * N(\text{CO}) * N_A}{N_{\text{photon}}} \quad (1)$$

where the N_A is the Avogadro constant and N(CO) is the yield of the evolved CO. The calculation of N_{electron} is based on the fact that two electrons are required to produce one molecule CO. The N_{photon} is calculated using the equation:

$$N_{\text{photon}} = \frac{[\text{Light intensity} * \text{Illumination area} * \text{Time}]}{\text{Average single photon energy}} \quad (2)$$

where the illumination area is controlled to 1 cm², and the average single photon energy (E_{photon}) is figured out using the equation:

$$E_{\text{photon}} = hc/\lambda \quad (3)$$

where h is the Planck constant, c indicates speed of light, and λ is the wavelength.

The incident light intensity was measured by a photometer (Newport, 840-C, USA). The total number of incident photons at 385 nm was estimated to be 6.16×10^{19} photon·h⁻¹ (Table S1).

In the photocatalytic degradation of MB, the photochemical reactor was illuminated using a 300 W Xenon arc lamp. In each test, 50 mg of the as-prepared sample was added into 100 mL MB solution (25 mg/L). Then, the suspension was stirred in the dark for 30 min to achieve the adsorption-desorption equilibrium. During irradiation, 5 mL of the suspension was taken out and centrifuged (10,000 rpm, 10 min) to remove the photocatalyst before measurement. The changes in

concentration of MB were monitored by measuring the UV-vis absorption of the suspension at 20 min interval. The absorbency at 665 nm was used to determine the concentration of MB by using a Shimadzu UV-2600 spectrometer.

2.5. Photo-electrochemical tests

Photo-electrochemical analysis was performed on a CHI760E electrochemical workstation in a standard three-electrode configuration with 0.5 M Na₂SO₄ solution as the electrolyte. FTO glass coated with the sample was used as the working electrode. 10 mg of photocatalyst and 10 μL of Nafion solution (5 wt%) were dispersed in 1 mL of ethanol by sonication to get a slurry mixture, after which the slurry was spin-coated onto the FTO. A Pt sheet and saturated calomel electrode (SCE) were used as the counter electrode and reference electrode, respectively. Transient photocurrent and electrochemical impedance spectroscopy (EIS) were measured at the open circuit potential. A sinusoidal ac perturbation of 5 mV was applied to the electrode over the frequency range from 0.01 Hz to 10 KHz.

2.6. Active species trapping and ESR experiments

The scavenging experiment was performed to explore the major reactive species in the photodegradation of MB. At the beginning of irradiation, 1 mM disodium edetate dihydrate (EDTA-2Na), 1 mM 1,4-benzoquinone (BQ) or 1 mM isopropanol (IPA) was respectively employed as the scavenger for h⁺, O₂⁻ and ·OH. Furthermore, presence of ·OH and O₂⁻ radicals was measured by the ESR technique using DMPO as the trapping agent. Before determining of the ·OH and O₂⁻ radicals, 10.0 mg catalyst was dispersed in 0.5 mL deionized water or 0.5 mL methanol, and then 50 μL DMPO was added with ultrasonic dispersion for 5 min. The signals were collected after 5 min of irradiation.

3. Results and discussion

3.1. Structure and morphology

The XRD patterns for CoZnAl-LDH (Fig. 1b) display characteristic features of hydrotalcite-type compounds, which are nearly the same as those of Co-Al LDH and Zn-Al LDH (JCPDS 51-0045). A similar phenomenon has also been observed for MgCoAl-LDH [41]. The diffraction peaks at 12.1°, 24.3°, 35.1°, 39.7° and 47.2° are assigned to the (003), (006), (009), (012) and (018) planes. The interlayer interval of the (003) plane is calculated to be ~0.764 nm, which indicates the intercalation of CO₃²⁻ in the gallery of CoZnAl-LDH [27]. g-C₃N₄ shows two basic diffraction peaks at approximately 12.8° and 27.6°, which reflect the in-plane structural packing motif and the inter-layer stacking of a conjugated aromatic system (JCPDS 87-1526), which can be well-indexed to the (100) and (002) planes of graphitic materials [42]. LDH/RGO/CN composites with different weight ratios of g-C₃N₄ have similar diffraction patterns with the pristine CoZnAl-LDH. Upon adding more g-C₃N₄, the diffraction peak at 27.6° becomes more obvious and stronger, thus indicating the existence of g-C₃N₄. Moreover, the (003) diffraction peak for all LDH/RGO/CN composites gradually shifts to a low angle, which demonstrates that some g-C₃N₄ and RGO may intercalate into the interlayer of CoZnAl-LDH nanosheets. The deviation of (003) peak of the XRD patterns can be further confirmed from its zoomed view (Fig. S1). Indeed, such a phenomenon also has been well documented in previous works concerning the modification of LDHs [43,44]. However, diffractions that belong to RGO cannot be observed in the hybrid due to its low content. In addition, LDH/CN without RGO also shows the characteristic peaks of g-C₃N₄ and CoZnAl-LDH, which confirms the coexistence of these two components. Raman spectroscopy was further conducted to demonstrate the presence of RGO. As shown in Fig. 1c, the absorptions in the range of 400–800 cm⁻¹ are attributed to the bare

CoZnAl-LDH. The Raman spectrum of RGO displays both D (the symmetry A1g k-point phonon) and G (the E2g phonon of sp² carbon atoms) bands at 1336 cm⁻¹ and 1564 cm⁻¹, respectively. For LDH/RGO/CN-2, all the characteristic peaks that belong to CoZnAl-LDH and RGO can be observed, which provides evidence for the existence of RGO. It is worth noting that the value of I_D/I_G for RGO increases from 0.95 to 1.07 after hybridization, and the G band of RGO moves to a high Raman shift by approximately 1588 cm⁻¹. This resulted from the strong interactions among RGO, g-C₃N₄ and CoZnAl-LDH, which lead to the formation of greater defects and disorders in RGO [45].

Fig. S2 shows the FT-IR spectra of g-C₃N₄, CoZnAl-LDH and LDH/RGO/CN composites. The bare g-C₃N₄ shows a series of peaks in the region of 1200–1650 cm⁻¹, which were assigned to the typical stretching modes of CN heterocycles. Absorption at 810 cm⁻¹ can be ascribed to the breathing mode of triazine units [46]. CoZnAl-LDH exhibits a characteristic absorption peak at 1357 cm⁻¹. This can be assigned to the asymmetrical stretching vibration of CO₃²⁻, which confirms the intercalated CO₃²⁻ in the interlayer [47,48]. For LDH/RGO/CN, the characteristic peaks of g-C₃N₄ and CoZnAl-LDH both were observed in the spectrum of LDH/RGO/CN-1, LDH/RGO/CN-2 and LDH/RGO/CN-3. Moreover, the absorptions were assigned to the CN heterocycle at 1200–1650 cm⁻¹, and the vibrational peaks that arose from the respiration of the triazine structure at 810 cm⁻¹ were gradually enhanced by the addition of additional g-C₃N₄. This demonstrates the successful combination of CoZnAl-LDH and g-C₃N₄.

As shown in the SEM image, g-C₃N₄ exhibits a bulky morphology with a typical lamellar packing structure (Fig. 2a). Bare CoZnAl-LDH with a superstructure was constructed from greater amounts of nanoplates (Fig. 2b), which are well dispersed with an average diameter approximately 5 μm. As displayed in Fig. 2c, the addition of g-C₃N₄ has some influence on the crystallinity and dispersibility of CoZnAl-LDH. Many g-C₃N₄ assemblies have emerged on the surfaces of CoZnAl-LDH, which causes a certain degree of agglomeration. Metal ions were hydrolysed and were gradually converted to CoZnAl-LDH under the effect of urea, when g-C₃N₄ was stripped into small-sized nanosheets and were deposited during a hydrothermal reaction. Fig. 2d–f show the CoZnAl-LDH/RGO/g-C₃N₄ composites that were prepared by using different amounts of g-C₃N₄ with a fixed weight value of RGO and CoZnAl-LDH. As was observed, the addition of g-C₃N₄ has a significant effect on the morphology of the hybrid. The content of g-C₃N₄ in LDH/RGO/CN-1 is low, so the appearance of this composite is similar to bare CoZnAl-LDH (Fig. 2d). For LDH/RGO/CN-2, the assemblies decrease. In particular, many fragmented nanosheets contribute to the formation of the scaffold, which makes LDH/RGO/CN-2 present an urchin-like hierarchical structure. When the amount of g-C₃N₄ increased to 0.15 g, the 3D architecture seemed to collapse for the LDH/RGO/CN-3 and bulky conglomerates that formed (Fig. 2f). Moreover, the EDS elemental mapping image for LDH/RGO/CN-2 (Fig. S3) shows the well-distributed C, N, O, Co, Zn and Al elements, which demonstrates that CoZnAl-LDH, RGO and g-C₃N₄ jointly contributed to the formation of the urchin-like hierarchical structure.

TEM shows that the bare CoZnAl-LDH is constructed by numerous nanoplates. Although this hierarchical structure is too thick to transmit the electron beam, the hollow interiors of the sample can still be identified by the contrast between the dark edges and the pale centres in Fig. S4. After the incorporation of g-C₃N₄ and RGO, LDH/RGO/CN-2 presents an urchin-like structure with a hollow cavity and a spiny external surface (Fig. 3a), which is in accordance with the SEM image above. g-C₃N₄ and RGO are uniformly distributed on CoZnAl-LDH, which was demonstrated by the HAADF-STEM image and the EDS elemental mapping images with the well-distributed six elements for LDH/RGO/CN-2 (Fig. 3b–h). The crystalline structure and elemental distributions of LDH/RGO/CN-2 were further investigated by high-resolution transmission electron microscopy (HRTEM) and the corresponding elemental mappings. As can be seen from the edge of a particle, lattice fringes with interlayer distances of 0.376 nm corresponding

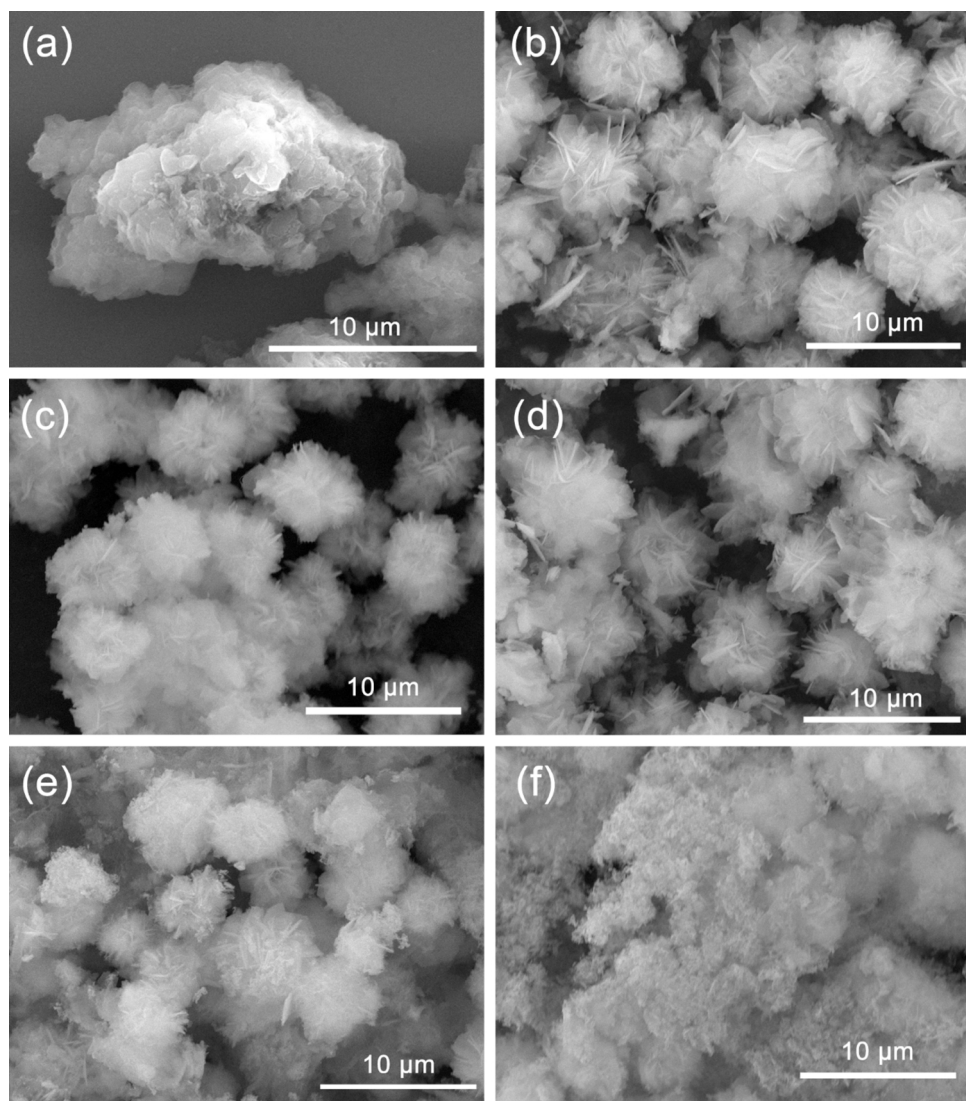


Fig. 2. FE-SEM images of (a) $\text{g-C}_3\text{N}_4$, (b) CoZnAl-LDH, (c) LDH/CN, (d) LDH/RGO/CN-1, (e) LDH/RGO/CN-2 and (f) LDH/RGO/CN-3.

to the (006) lattice plane of CoZnAl-LDH and 0.213 nm corresponding to the typical (100) planes of RGO can be indexed; besides the existence $\text{g-C}_3\text{N}_4$, the composition of LDH/RGO/CN-2 can be further confirmed (Fig. 3i-j). Moreover, the distinct interfaces among the three phases can be identified clearly. The HAADF-STEM of a spiny external surface and the corresponding EDS elemental mapping images of C, N, O, Co, Zn and Al elements clearly illustrate the homogeneous hybridization of CoZnAl-LDH, RGO and $\text{g-C}_3\text{N}_4$ (Fig. 3l-q).

The content of CoZnAl-LDH, RGO and $\text{g-C}_3\text{N}_4$ in the LDH/RGO/CN-2 composite was further determined by thermogravimetric (TG) analysis. As shown in Fig. S5, the pristine CoZnAl-LDH displays two main steps of weight loss. The first weight loss below 250 °C was attributed to the desorption of surface adsorbed and interlayer water molecules. The second weight loss between 250–350 °C corresponds to the decomposition of interlayer carbonate ions. Weight loss above 350 °C can be assigned to the dehydration of hydroxide plates accompanied by the collapse of the layer structure [49]. The char yield of CoZnAl-LDH is 72.4 wt%. For RGO, two significant weight loss stages can be observed. The adsorbed water evaporates below 200 °C, while the subsequent weight loss is due to the decomposition of residual oxygen-containing groups [50]. The total weight loss reaches 33.9 wt%. $\text{g-C}_3\text{N}_4$ exhibits a steep deposition around 500–700 °C, and it is fully decomposed with nearly no residue. Therefore, the actual content of CoZnAl-LDH, RGO and $\text{g-C}_3\text{N}_4$ in LDH/RGO/CN-2 can be determined as 65 wt%, 27 wt%

and 8 wt%, respectively. Moreover, the zeta potential measurement was also performed to illustrate the formation mechanism of this special urchin-like ternary composite (Fig. S6). CoZnAl-LDH exhibits positive zeta potential value, whereas RGO and $\text{g-C}_3\text{N}_4$ are both negative charged. Although some of the Co^{2+} , Zn^{2+} and Al^{3+} may interact with the RGO and $\text{g-C}_3\text{N}_4$ via electrostatic effect, a great number of metal cations mainly participate in the construction of CoZnAl-LDH due to the presence of larger amounts of nitrates compared with that of RGO and $\text{g-C}_3\text{N}_4$. The urchin-like scaffold with a positive zeta potential can be built by the self-assembly of bare CoZnAl-LDH, during which time RGO and $\text{g-C}_3\text{N}_4$ are integrated through electrostatic interactions. A significant shift in the zeta potential after hybridization is noticed owing to the coverage of negatively charged RGO and $\text{g-C}_3\text{N}_4$ over CoZnAl-LDH.

The coexistence of C and N in $\text{g-C}_3\text{N}_4$ can be confirmed by XPS survey spectrum (Fig. 4a). CoZnAl-LDH is composed of Co, Zn, Al, C and O elements. For LDH/RGO/CN-2, the survey spectrum shows signals of Co, Zn, Al, C, N and O elements, which demonstrates the hybridization of CoZnAl-LDH and $\text{g-C}_3\text{N}_4$. Fig. 4b shows the C1s high-resolution spectra of the three samples. The C1s XPS spectrum of $\text{g-C}_3\text{N}_4$ can be deconvoluted into three peaks at 284.6 eV, 286.1 eV and 287.9 eV, which corresponding to adventitious carbon, C-NH_2 on the edge of heptazine units and sp^2 -bonded carbon in N-containing aromatic rings ($\text{N}-\text{C}=\text{N}$) [51]. Since CoZnAl-LDH contains a large number of carbonates, its C1s can be dissociated into carbon contamination (284.6 eV),

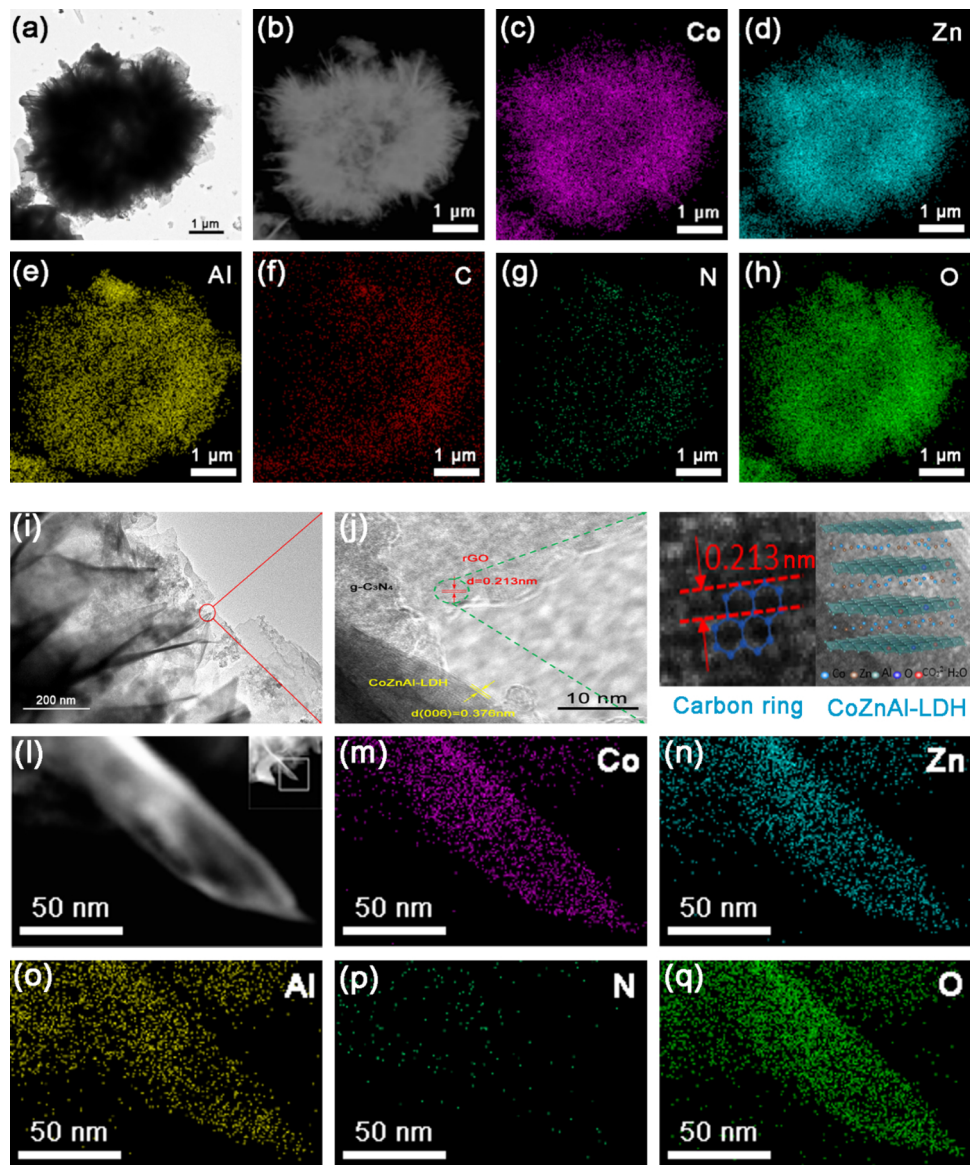


Fig. 3. (a,i) The whole and edge TEM images of an LDH/RGO/CN-2 particle; (b–l, l–q) HAADF-STEM images and EDS elemental mapping images of LDH/RGO/CN-2 and the spiny external surface. The insert of (l) shows the selected region for HAADF-STEM and EDS elemental mapping images; (j) HRTEM image of the selected area for LDH/RGO/CN-2. The selected areas represent carbon rings of RGO and layer structure of CoZnAl-LDH, respectively.

C–O (288.1 eV) and C=O (292.0 eV). For LDH/RGO/CN-2, five peaks for adventitious and graphitic carbon (284.6 eV), C–NH₂ (286.3 eV), C–O (287.8 eV), N=C=N (288.2 eV) and C=O (291.8 eV) can be identified. The increased signal for sp^2 -bonded carbon indicates the addition of RGO. Compared to the bare CoZnAl-LDH, the intensity of XPS peaks corresponding to carbonates are obviously decreased. It signifies the replacement of carbonates by the intercalation of g-C₃N₄ and RGO, which is in accordance with the above XRD analyses. Moreover, the binding energies of carbon species belonging to g-C₃N₄ and CoZnAl-LDH in the hybrid have changed, thus indicating strong chemical and electronic coupling interactions among g-C₃N₄, RGO and CoZnAl-LDH. Fig. 4c shows the N1s high-resolution spectra for g-C₃N₄ and LDH/RGO/CN-2. Four peaks at 397.3 eV, 398.9 eV, 400.1 eV and 402.8 can be identified for g-C₃N₄, which correspond to the nitrogen-bonded species of C=N=C, N–(C)₃, C–NH₂ and C–N–H, respectively [52]. The N1s of LDH-RGO-CN-2 can be divided into four peaks which are in good accordance with g-C₃N₄. Fig. 4d-f show the high-resolution spectra of Co2p, Zn2p and Al2p, respectively. For CoZnAl-LDH, the binding energies at 780.7 eV and 796.6 eV are assigned to Co 2p_{3/2} and

Co 2p_{1/2}, respectively. The appearance of satellite peaks at 787.3 eV and 803.2 eV signifies the presence of high-spin divalent Co²⁺ in this hydrotalcite [53]. After doping with RGO and g-C₃N₄, the binding energy of Co 2p_{3/2} and Co 2p_{1/2} shifts to lower values of 780.4 eV and 796.3 eV in LDH-RGO-CN-2, and the satellite peaks can still be observed. Fig. 4e shows the spin-orbit doublet splitting of the Zn element, the binding energies of Zn 2p_{1/2} and Zn 2p_{3/2} are located at 1044.3 eV and 1021.1 eV in CoZnAl-LDH, which is consistent with divalent Zn²⁺ [54]. Moreover, trivalent Al³⁺ can be determined as the binding energy at 73.7 eV. It is worth noting that the binding energies of Zn2p and Al2p in LDH/RGO/CN-2 are also slightly decreased compared with that of the pristine CoZnAl-LDH. Generally, in the XPS spectra, the shift of binding energy indicates a strong interfacial interaction between the different components. The increase of binding energy means there is a weakened electron screening effect due to the decrease of the electron concentration, whereas the decrease of this value implies an increase in the electron concentration. According to the variation of binding energies for LDH/RGO/CN-2 compared with that of the constituents, a built-in electric field is prescribed between CoZnAl-LDH and g-C₃N₄.

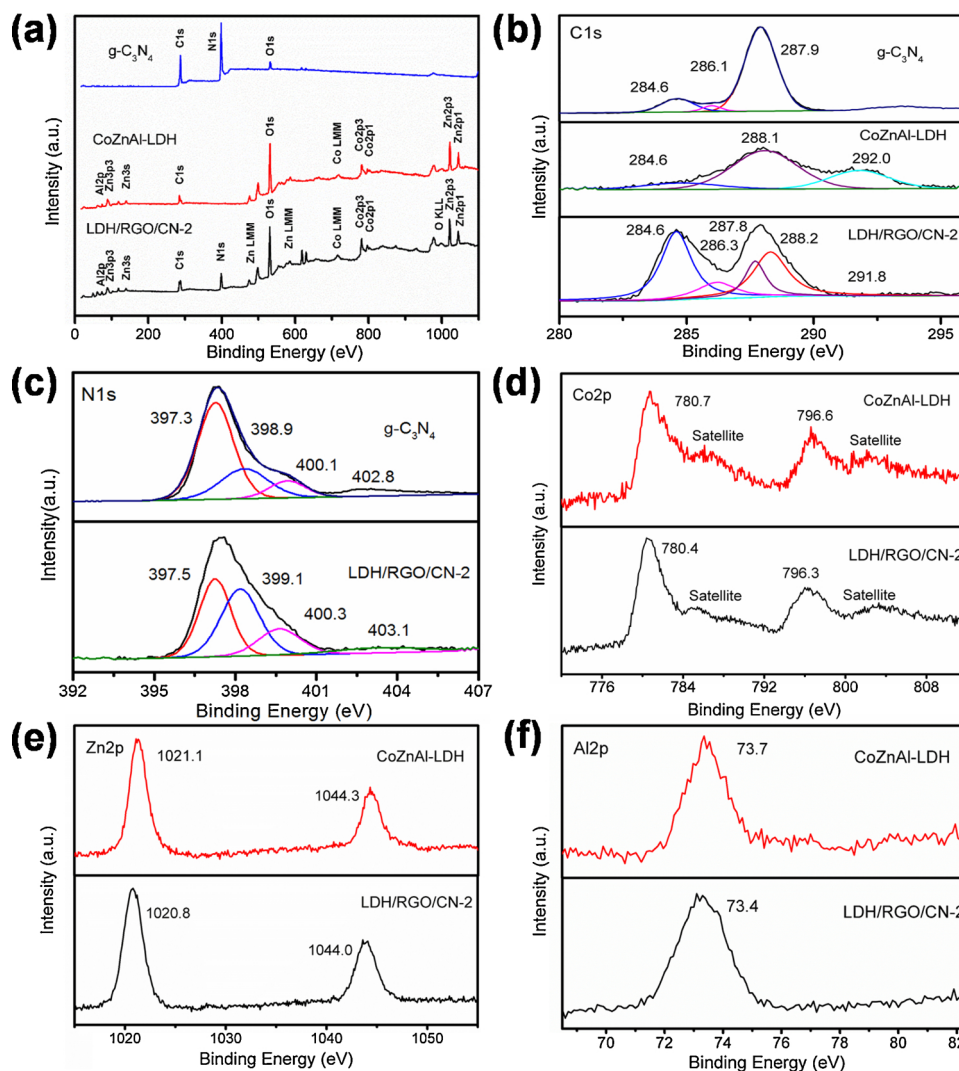


Fig. 4. (a) XPS survey spectra of CoZnAl-LDH, g-C₃N₄ and LDH/RGO/CN-2; (b) C1s, (c) N1s, (d) Co2p, (e) Zn2p and (f) Al2p core-level XPS spectra, respectively.

The efficient charge migration and separation can thus be suggested for LDH/RGO/CN-2 under irradiation.

The representative N₂ adsorption-desorption isotherms (Fig. S7) of CoZnAl-LDH, LDH/CN and LDH/RGO/CN-2 are all of type IV with H₃-type hysteresis loops ($0.7 < P/P_0 < 1.0$), which indicates the formation of a mesoporous structure due to the aggregation of nanoplates [44,55]. The BET specific surface area of CoZnAl-LDH, LDH/CN and LDH/RGO/CN-2 are 11.7 m²/g, 13.1 m²/g and 13.5 m²/g, respectively. Accordingly, the pore-size distributions (shown in the inset of Fig. S7) display a relatively wide range from 20 to 200 nm, which demonstrates the presence of mesopores and macropores. The most probable apertures of CoZnAl-LDH, LDH/CN and LDH/RGO/CN-2 are 36.8 nm, 38.9 nm and 38.2 nm, respectively. These results suggest that the loading of g-C₃N₄ and RGO has no obvious effect on the specific surface area and pore size of CoZnAl-LDH. Combined with the TEM images of LDH/RGO/CN-2, it can be supposed that the intimate interfaces among g-C₃N₄, RGO and CoZnAl-LDH would avail the electron transfer between CoZnAl-LDH and g-C₃N₄ during photocatalysis, and the separation of light-induced electrons and holes can be promoted.

Fig. 5a displays the photoabsorption behaviours of the prepared CoZnAl-LDH, g-C₃N₄ and LDH/RGO/CN samples. CoZnAl-LDH shows obvious absorptions in the ultraviolet region from 200 nm to 280 nm and in the visible light region from 450 nm to 680 nm, which can be attributed to the presence of metal cations. g-C₃N₄ exhibits absorptions from 300 nm to 470 nm due to the narrow intrinsic band gap [56], and

it has an obvious absorption band edge at approximately 450 nm. For the LDH-CN composite, its absorption range in the UV range is obviously wider than that of the bare CoZnAl-LDH. Similar to CoZnAl-LDH, LDH/CN also shows an absorption band in the visible light range, which confirms the co-existence of CoZnAl-LDH and g-C₃N₄. As seen from the insert picture in Fig. 5a, after the addition of RGO, the appearance of three composite samples becomes significantly darker. The presence of a carbon substance results in a significant up-shift of the absorption spectra. It is worth noting that LDH/RGO/CN-2 exhibits the strongest absorptions, although the weight ratio of RGO in LDH/RGO/CN-2 is lower than that of LDH/RGO/CN-1. The special spiny external surface and hollow inner cavity endow LDH/RGO/CN-2 with significantly enhanced light harvesting capacity. For LDH/RGO/CN-3, the decreased ratio of RGO and the collapsed structure lead to a decrease in the absorptions. In addition, we calculated the bandgap energy of g-C₃N₄ and CoZnAl-LDH based on the UV-DRS and the following empirical formula: $\text{E}_{\text{h}} = A(\hbar\nu - E_g)^{n/2}$. As shown in Fig. 5b, the estimated band gaps for g-C₃N₄ and CoZnAl-LDH are 2.71 eV and 2.60 eV, respectively.

3.2. Photocatalytic CO₂ reduction

The photocatalytic performance of CO₂ conversion over the as-prepared samples was investigated in the presence of few waters as the sacrificial agent. CO and CH₄ are generated as the products. Meanwhile,

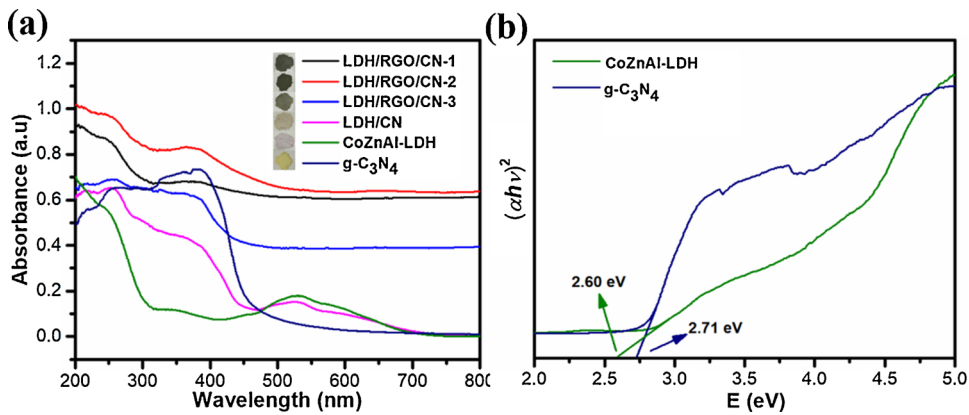


Fig. 5. (a) UV–vis diffuse reflectance spectra of the different samples (insert: digital pictures); (b) The band gap of the synthesized CoZnAl-LDH and g-C₃N₄.

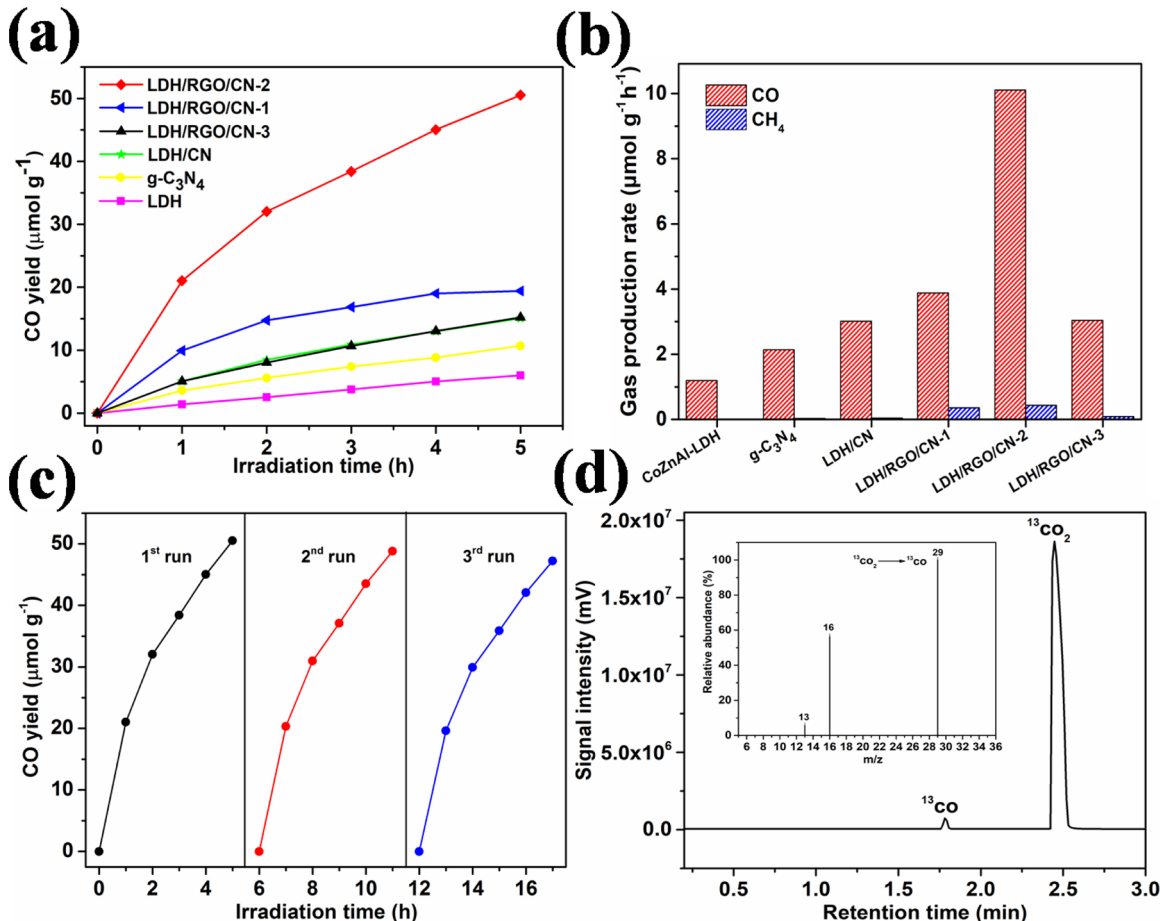


Fig. 6. (a,b) Time evolutions of CO and average gas production rates over different catalysts; (c) Recycling test of photocatalytic CO production over LDH/RGO/CN-2; (d) The isotope analysis of ¹³CO using ¹³CO₂ as carbon source by GC-MS.

O₂ has evolved as the oxidative half-reaction, which can be demonstrated by a gradual increase in the ratio of oxygen to nitrogen (Fig. S8). As shown in the time evolution curves of CO and CH₄ (Fig. 6a and Fig. S9), the yield of CO is far beyond CH₄ after 5 h of irradiation for all the photocatalysts. By comparing the main product of CO, its yield on the bare CoZnAl-LDH and g-C₃N₄ is 5.99 $\mu\text{mol g}^{-1}$ and 10.69 $\mu\text{mol g}^{-1}$, respectively. The CO production for LDH/CN significantly increased to 15.06 $\mu\text{mol g}^{-1}$. After adding RGO, the production of CO for the ternary composite samples further increased. CO production for LDH/RGO/CN-3 and LDH/RGO/CN-1 is 15.19 $\mu\text{mol g}^{-1}$ and 19.39 $\mu\text{mol g}^{-1}$, which increased by 0.8% and 29% more than that of the binary system of LDH/CN. For LDH/RGO/CN-2, the production of CO reaches

50.53 $\mu\text{mol g}^{-1}$. Fig. 6b compares the overall CO and CH₄ evolution rates for CoZnAl-LDH, g-C₃N₄, LDH/CN and the three ternary composite samples. The average CO production rates of the bare CoZnAl-LDH and g-C₃N₄ are 1.19 $\mu\text{mol g}^{-1} \text{h}^{-1}$ and 2.13 $\mu\text{mol g}^{-1} \text{h}^{-1}$, respectively. After hybridization, the production rate reaches 3.01 $\mu\text{mol g}^{-1} \text{h}^{-1}$ for LDH/CN. Furthermore, when RGO is introduced as the electron mediator, LDH/RGO/CN-2 exhibits a remarkable enhancement of the photocatalytic performance. The average CO production rate achieves 10.11 $\mu\text{mol g}^{-1} \text{h}^{-1}$, which is 3.4 and 8.5 times that of LDH/CN and the bare CoZnAl-LDH, respectively. The selectivity of the ternary hybrid towards CO production is impressively beyond 96%, and the apparent quantum yield of LDH/RGO/CN-2 achieves 0.45% at $\lambda = 385$ nm. After

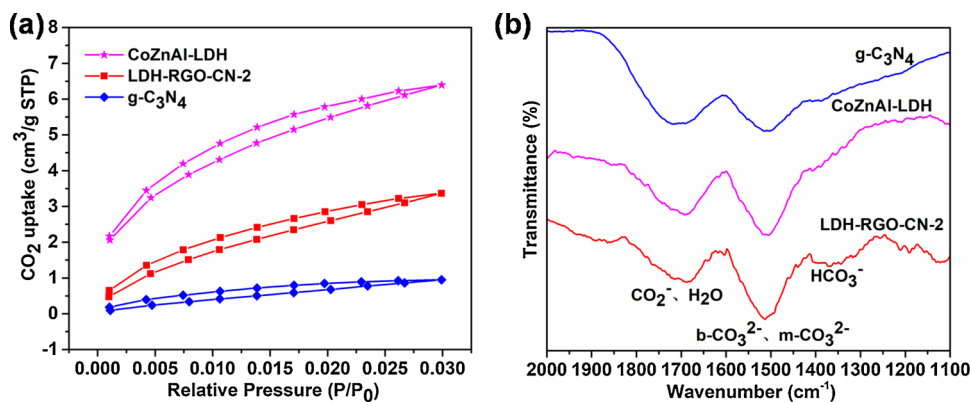


Fig. 7. (a) CO₂ adsorption-desorption isotherms and (b) *in situ* FTIR spectra of adsorbed CO₂ over different samples.

three cycles of recycling tests, LDH/RGO/CN-2 shows no significant decrease in the yield of CO (Fig. 6c), which confirms its favourable photostability. LDH/RGO/CN-2 shows the highest photocatalytic activity mainly for the following two reasons. On the one hand, the addition of RGO promotes the charge transfer between g-C₃N₄ and CoZnAl-LDH, which efficiently enhances the separation of photo-generated charge carriers. On the other hand, LDH/RGO/CN-2 possesses a uniform and intact urchin-like structure. The spiny external surface and hollow inner cavity are in favour of mass transfer for reactants and products, light harvesting and utilization. The low content of g-C₃N₄ of LDH/RGO/CN-1 and the collapsed structure of LDH/RGO/CN-3 result in their decreased photocatalytic activities compared with that of LDH/RGO/CN-2. Control experiments were performed without light, CO₂ or photocatalyst. No appearance of production was detected, proving that the photocatalytic CO₂ reduction was driven by irradiation with the photocatalysts. Additionally, isotopically labeled ¹³CO₂ experiment was conducted on gas chromatography-mass spectrometry for determination of the products from photoreduction of LDH/RGO/CN-2 (Fig. 6d). A strong signal at *m/z* = 29 attributed to ¹³CO can be detected, which confirms that the carbon source of CO is the introduced CO₂.

3.3. Mechanism considerations

Absorption and activation of CO₂ are prerequisites for the photocatalytic conversion. A high reduction efficiency is based on the enough retention time of CO₂ molecules on the surfaces of photocatalysts [57,58]. As depicted in Fig. 7a, the bare g-C₃N₄ shows a weak adsorption capacity for CO₂ molecules. In contrast, CoZnAl-LDH exhibits the strongest adsorption performance among the samples. The inherent basic character endows great potential for photocatalytic CO₂ conversion to this kind of hydrotalcite. The hierarchical structure of CoZnAl-LDH made a significant contribution to the CO₂ capture, as it facilitated the diffusion of CO₂ molecules over the assemblies and, therefore, enhanced the utilization of surface active sites. LDH/RGO/CN-2 based on the combination of CoZnAl-LDH and g-C₃N₄ shows a moderate adsorption performance, whereas coated RGO and g-C₃N₄ covered many of the strong adsorption sites. To check the adsorbed states of CO₂, the *in-situ* Fourier transform infrared spectroscopy (FT-IR) analysis was conducted on g-C₃N₄, CoZnAl-LDH and LDH/RGO/CN-2 under the same conditions as the photocatalytic reaction. As shown in Fig. 7b, the band around 1680 cm⁻¹ is resulted from the asymmetric vibration of bicarbonate (CO₂⁻) and adsorbed H₂O. The absorption belonging to CO₂⁻, which represents the interactions between oxygen from CO₂ and the surface atoms from the catalyst, commonly forms via the one electron transfer from photocatalyst to the surface-coordinated CO₂ molecule [59]. Absorptions ranging from 1500 cm⁻¹ to 1580 cm⁻¹ are assigned to monodentate, bidentate carbonates (m-CO₃²⁻ and b-CO₃²⁻) and bicarbonate (HCO₃⁻) coordinated on the photocatalyst

surfaces [60,61]. For g-C₃N₄, the intensity of these two absorption bands are nearly the same, whereas the absorptions of b-CO₃²⁻ and m-CO₃²⁻ for CoZnAl-LDH are obviously enhanced. This indicates more straightforward interactions between the photocatalyst and CO₂ molecule, thus implying a strong chemical activation capacity towards CO₂ caused by the Lewis acid nature of Co²⁺, Zn²⁺ and Al³⁺. Upon compositing with g-C₃N₄ and RGO, LDH/RGO/CN-2 shows further enhanced chemical interactions with CO₂ due to the synergistic action among the constituents. Chemical activation towards CO₂ will decrease the bonding energy of O=C=O and reduce the reaction barrier, thus improving the conversion efficiency for photocatalysis [62–64].

To elucidate the improved CO₂ photoreduction performance of LDH/RGO/CN composites, especially LDH/RGO/CN-2, photoelectrochemical characterizations were performed. The charge transfer dynamics for CoZnAl-LDH and LDH/RGO/CN-2 were investigated by time-resolved photoluminescence (TRPL) decay spectra (Fig. 8a). Evidently, the average lifetime of the photogenerated charge carries in LDH/RGO/CN-2 (4.29 ns) is strikingly more prolonged than that of CoZnAl-LDH (0.58 ns). It is well-known that a longer lifetime of electrons and holes implies a high probability for participation in photocatalytic reaction and improved activity [65,66]. As shown in Fig. 8b, strong PL emission peaks are observed for the bare g-C₃N₄ and CoZnAl-LDH, which are located around 460 nm and 450 nm respectively. The fast recombination of photogenerated electron-hole pairs severely restricts their photocatalytic activities. Compared with them, LDH/RGO/CN-2 exhibits a weak PL intensity, thus illustrating the decreased recombination of photogenerated electrons and holes. The charge transfer between CoZnAl-LDH and g-C₃N₄ is remarkably promoted after the addition of RGO. Transient photocurrent responses for g-C₃N₄, CoZnAl-LDH, and LDH/RGO/CN composites were recorded by switching the irradiation light on and off for several cycles to further reveal their photocatalytic activities (Fig. 8c). LDH/RGO/CN composites display significantly improved photocurrent compared with individual g-C₃N₄ and CoZnAl-LDH. LDH/RGO/CN-2 shows the highest photocurrent intensity, thus confirming it as having the strongest light harvesting capacity and the best separation efficiency of electron-hole pairs. Notably, an anodic photocurrent spike emerges in all the photocurrent curves once the light is turned on, which results from the vast recombination of photogenerated electron-hole pairs at the initial time of irradiation. Then, the photocurrent decreases and remains almost constant due to the equilibration between the separation and recombination of electron-hole pairs [67]. To further evaluate the charge transfer property, electrochemical impedance spectroscopy (EIS) was employed. In Fig. 8d, the arc radius of the Nyquist circle for LDH/RGO/CN-2 is the smallest among all of the samples, thus implying the lowest resistance for the charge transfer. The effective transport of electrons and holes among the components can retard the recombination of them, and therefore numerous free charge carriers will participate in the reactions.

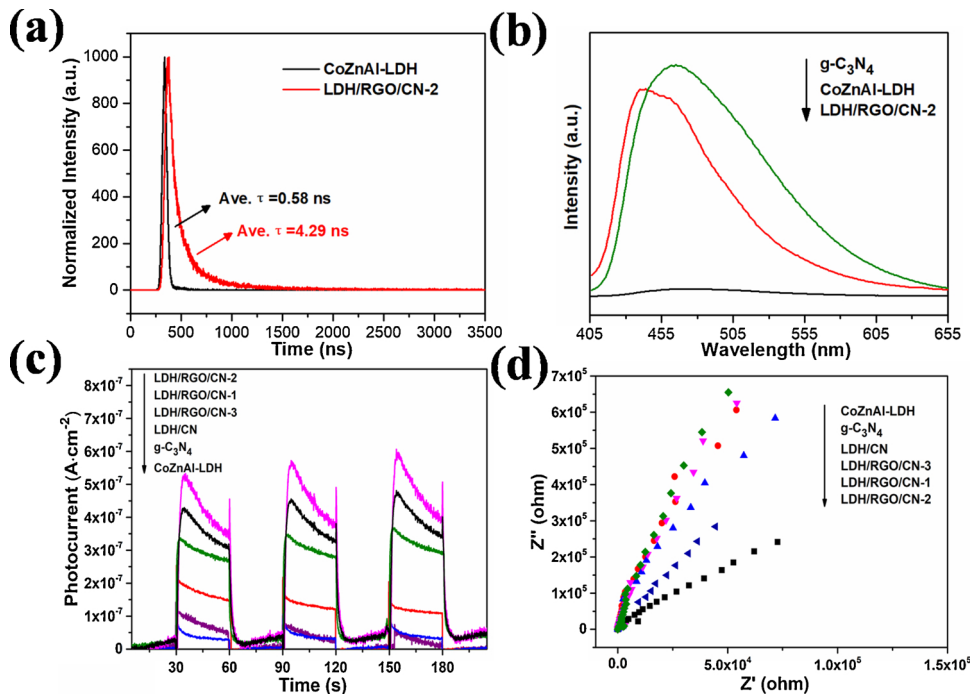


Fig. 8. (a) Time-resolved fluorescence decay traces; (b) Photoluminescence spectra of the samples (the excitation wavelength is 400 nm); (c) Transient photocurrent responses and (d) electrochemical impedance spectra (EIS) of the as-prepared samples.

The band structure of CoZnAl-LDH and g-C₃N₄ was further determined for an investigation of the transfer path of light-induced electrons and holes. From Fig. S10, the valence band (VB) energy levels of g-C₃N₄ and CoZnAl-LDH are estimated to be ~2.20 and ~0.51 eV below the Fermi level. According to Mott-Schottky measurements (Fig. S11a and S11b), the flat-band potentials approximating to the Fermi level of g-C₃N₄ and CoZnAl-LDH can be prescribed as -0.71 V and 1.94 V (vs. NHE) [68]. Moreover, g-C₃N₄ and CoZnAl-LDH can be determined as the n-type semiconductor and the p-type semiconductor, respectively. The p-n heterojunction was thus formed after the hybridization of these two materials. The direction of built-in electric field in LDH/RGO/CN-2 is in favour of the construction of a Z-scheme heterojunction, which confirms the XPS analyses. In combination with the band-gap values that were determined in the UV-DRS analyses, the conduction band (CB) and valence band (VB) positions of CoZnAl-LDH can be determined as -0.15 V and 2.45 V, respectively. Meanwhile, the CB and VB positions of g-C₃N₄ are calculated to be -1.22 V and 1.49 V, which have good consistency with the reported values [69]. The E_{CB} of g-C₃N₄ is negative enough for the reduction of CO₂ to CO (E^o = -0.53 V vs NHE, pH = 7) [70]. Thus, from a thermodynamic viewpoint, g-C₃N₄ can be photoexcited and then converts CO₂ to CO. For CoZnAl-LDH, the strong accumulation and chemical activation capacities towards CO₂ decrease the reaction barrier for CO₂ reduction. Combined with irradiation by a full-spectrum solar simulator of the xenon lamp, the evolution of CO can be detected. However, the photocatalytic CO yields of bare CoZnAl-LDH and g-C₃N₄ are low due to the rapid recombination of electron-hole pairs. Based on the above analyses, the efficient charge transfer between CoZnAl-LDH and g-C₃N₄ in the LDH/RGO/CN composites should be respected as the fundamental contribution to the improvement of CO₂ conversion.

The photodegradation experiment for methylene blue and the detection of reactive species during the process were conducted for the investigation of the charge flow for the LDH/RGO/CN hybrid. As shown in Fig. 9a, the degradation efficiencies of bare CoZnAl-LDH and g-C₃N₄ are only 17% and 48% after 2 h of irradiation. The weak light harvesting capacity and rapid recombination of electrons and holes intensely restrict their photocatalytic activities. LDH/CN shows an

improved degradation efficiency for 57%, which is consistent with the trend of CO₂ photocatalytic conversion. For LDH/RGO/CN-2, the degradation efficiency reaches 87% after 1 h, and the dye is completely removed after 2 h with a degradation efficiency beyond 99%. The pseudo first-order kinetic equation for degradation (Fig. S12) shows a good linear relationship between ln(C₀/C) and t. LDH/RGO/CN-2 shows the highest photocatalytic degradation rate with a kinetic constant of k_{app} = 0.0211 min⁻¹. The trapping experiments were performed to reveal the roles of possible reactive species in photodegradation. Isopropanol (IPA) was used to eliminate the hydroxyl radical ('OH). The superoxide radical ('O₂⁻) and the hole (h⁺) were removed by benzoquinone (BQ) and ethylenediaminetetraacetic acid (EDTA-2Na), respectively [71,72]. As shown in Fig. 9b, MB decomposition over LDH/RGO/CN-2 is severely suppressed by the addition of BQ. When EDTA-2Na is added, the photocatalytic degradation efficiency is also significantly reduced by 31%. Therefore, 'O₂⁻ and h⁺ are the main active species for the degradation of LDH/RGO/CN-2. As depicted in Fig. 9e, if the photoinduced charge carriers were transported through a conventional type-II heterojunction route, the photogenerated electrons of g-C₃N₄ would migrate to the CB of CoZnAl-LDH, while the holes on the CoZnAl-LDH transfer to VB of g-C₃N₄. The E_{CB} of CoZnAl-LDH is not negative enough to produce 'OH (O₂/⁻O₂, -0.33 eV vs. NHE), and the E_{VB} of g-C₃N₄ is also not positive enough to produce 'OH ('OH/H₂O, +2.40 eV vs. NHE). Therefore, the type-II heterojunction mechanism is not suitable for the LDH/RGO/CN-2 hybrid.

To validate the Z-scheme charge transfer mechanism, the electron spin resonance (ESR) measurement was carried out by using 5,5-dimethyl-1-pyrroline-N-oxide (DMPO) as a spin-trapping reagent. 'O₂⁻ is generated by the electron injection to dissolved O₂ in methanol, whereas 'OH evolves based on the electron extraction from OH⁻ in water. These two transient radicals will transform to DMPO-'OH and DMPO-'O₂⁻ adducts which are stable radicals that are suitable for ESR detection [73,74]. As shown in Fig. 9c, four characteristic peaks with the intensity ratio of 1:2:2:1 for DMPO-'OH adducts are observed for CoZnAl-LDH, g-C₃N₄ and LDH/RGO/CN-2. This indicates that 'OH radicals are generated on the three samples upon irradiation. Based on the

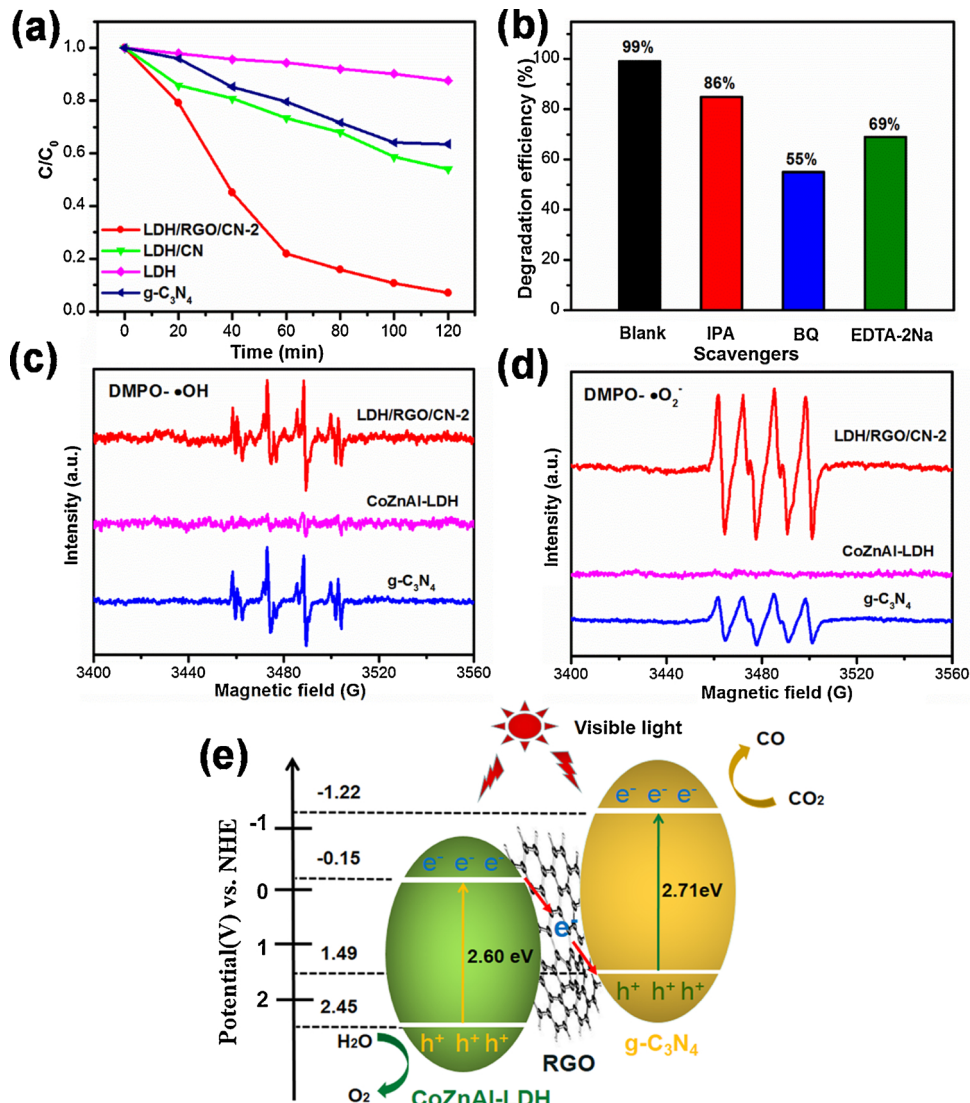


Fig. 9. (a) Degradation curves of MB for different samples under visible light; (b) Effect of different scavengers on the photocatalytic efficiency of LDH/RGO/CN-2; (c,d) ESR spectra of DMPO-·OH and DMPO-·O₂⁻ adducts over different samples after irradiation; (e) Schematic diagram of the possible photocatalytic mechanism for LDH/RGO/CN.

band structure of g-C₃N₄ and the previous report, ·OH for g-C₃N₄ is generated by further reduction of ·O₂⁻, which is an indirect approach [75]. In contrast with the weak signal for bare CoZnAl-LDH, LDH/RGO/CN-2 exhibits much higher peaks due to its high oxidation capacity. Meanwhile, the six characteristic peaks assigned to DMPO-·O₂⁻ adducts are presented for g-C₃N₄ and LDH/RGO/CN-2 (Fig. 9d). No signal is observed for the pure CoZnAl-LDH, which is in accordance with the potential of its CB. It is worth noting that the intensity of DMPO-·O₂⁻ signals for LDH/RGO/CN-2 is significantly stronger than that of bare g-C₃N₄, which implies an enhanced reduction capability. According to the above results of ESR, LDH/RGO/CN-2 is more favourable for the production of ·O₂⁻ and ·OH than its corresponding constituents. Based on the increased charge separation efficiency and the enhanced oxidizing and reducing capacities, the Z-scheme mechanism for LDH/RGO/CN-2 can be confirmed.

The band alignment of the LDH/RGO/CN hybrid and the detailed Z-scheme mechanism are illustrated in Fig. 9e and is explained as follows. Under irradiation, CoZnAl-LDH and g-C₃N₄ are both excited to generate the electrons and holes. Through the conduction of RGO, electrons on the CB of CoZnAl-LDH transfer to the VB of g-C₃N₄ and finally combine with the photogenerated holes on the VB of g-C₃N₄. This can lead to the

accumulation of electrons and holes on the CB of g-C₃N₄ and the VB of CoZnAl-LDH. Consequently, the oxidizability and reducibility of the photocatalyst are promoted. For LDH/RGO/CN-2, the Z-scheme charge transfer process efficiently improves the separation of photoinduced electrons and holes, combining with the unique urchin-like hierarchical morphology, the photocatalytic performance is significantly enhanced.

4. Conclusions

In summary, a unique urchin-like LDH/RGO/CN Z-scheme photocatalyst was developed with the hydrothermal synthesis of CoZnAl-LDH and the *in-situ* loading of RGO and g-C₃N₄. The special 3D urchin-like hierarchical structure endows LDH/RGO/CN with an enhanced light harvesting capacity, which causes more photons to participate in photocatalytic CO₂ conversion. The formation of a Z-scheme heterojunction not only restricts the recombination of photoinduced electron-hole pairs, but also promotes the oxidizability and reducibility of CoZnAl-LDH and g-C₃N₄. Furthermore, the improved chemical adsorption and activation towards CO₂ for the photocatalyst reduce the reaction barrier for CO₂ photoreduction. Based on these synergistic actions, LDH/RGO/CN exhibits enhanced performance in the photocatalytic CO₂

conversion to CO with excellent selectivity. This study provides a new strategy for the fabrication of LDHs-based photocatalysts in CO₂ conversion by synchronously combining the characteristics of intense light harvesting capacity, efficient separation of charge carriers, enhanced adsorption and chemical activation towards reactants.

Acknowledgments

We are grateful to the National Natural Science Foundation of China (51303083, 21673001), the China Postdoctoral Science Foundation (2017m621708), the Natural Science Foundation of Jiangsu Province for Distinguished Young Scholars (BK20170038) and the Fundamental Research Funds for the Central Universities (30917011310) for financial support.

Appendix A. Supplementary data

Supplementary material related to this article can be found, in the online version, at doi:<https://doi.org/10.1016/j.apcatb.2019.117771>.

References

- [1] S.H. Knox, C. Sturtevant, J.H. Matthes, L. Koteen, J. Verfaillie, D. Baldocchi, Agricultural peatland restoration: effects of land-use change on greenhouse gas (CO₂ and CH₄) fluxes in the Sacramento-San Joaquin Delta, *Glob. Change Biol. Bioenergy* 21 (2015) 750–765, <https://doi.org/10.1111/gcb.12745>.
- [2] G.L. Stephens, B.H. Kahn, M. Richardson, The super greenhouse effect in a changing climate, *J. Clim.* 29 (2016) 5469–5482, <https://doi.org/10.1175/JCLI-D-15-0234.1>.
- [3] M. Mikkelsen, M. Jorgensen, F.C. Krebs, The teraton challenge. A review of fixation and transformation of carbon dioxide, *Energy Environ. Sci.* 3 (2010) 43–81, <https://doi.org/10.1039/B912904a>.
- [4] J. Kou, C. Lu, J. Wang, Y. Chen, Z. Xu, R.S. Varma, Selectivity enhancement in heterogeneous photocatalytic transformations, *Chem. Rev.* 117 (2017) 1445–1514, <https://doi.org/10.1021/acs.chemrev.6b00396>.
- [5] W. Tu, Y. Zhou, Z. Zou, Photocatalytic conversion of CO₂ into renewable hydrocarbon fuels: state-of-the-art accomplishment, challenges, and prospects, *Adv. Mater.* 26 (2014) 4607–4626, <https://doi.org/10.1002/adma.201400087>.
- [6] L. Shi, T. Wang, H. Zhang, K. Chang, J. Ye, Electrostatic self-assembly of nanosized carbon nitride nanosheet onto a zirconium metal-organic framework for enhanced photocatalytic CO₂ reduction, *Adv. Funct. Mater.* 25 (2015) 5360–5367, <https://doi.org/10.1002/adfm.201502253>.
- [7] J.L. White, M.F. Baruch, J.E. Pander III, Y. Hu, I.C. Fortmeyer, J.E. Park, T. Zhang, K. Liao, J. Gu, Y. Yan, T.W. Shaw, E. Abelev, A.B. Bocarsly, Light-driven heterogeneous reduction of carbon dioxide: photocatalysts and photoelectrodes, *Chem. Rev.* 115 (2015) 12888–12935, <https://doi.org/10.1021/acs.chemrev.5b00370>.
- [8] S.N. Habireuttinger, L. Schmidt-Mende, J.K. Stolarczyk, Photokatalytische reduktion von CO₂ an TiO₂ und anderen halbleitern, *Angew. Chem. Int. Ed.* 125 (2013) 7516–7557, <https://doi.org/10.1002/ange.201207199>.
- [9] M. Abdellah, A.M. El-Zohry, L.J. Antila, C.D. Windle, E. Reisner, L. Hammarstrom, Time-resolved IR spectroscopy reveals a mechanism with TiO₂ as a reversible electron acceptor in a TiO₂-Re catalyst system for CO₂ photoreduction, *J. Am. Chem. Soc.* 139 (2017) 1226–1232, <https://doi.org/10.1021/jacs.6b11308>.
- [10] M. Pirhashemi, A. Habibi-Yangjeh, S.R. Pouran, Review on the criteria anticipated for the fabrication of highly efficient ZnO-based visible-light-driven photocatalysts, *J. Ind. Eng. Chem.* 62 (2018) 1–25, <https://doi.org/10.1016/j.jiec.2018.01.012>.
- [11] M. Shekofteh-Gohari, A. Habibi-Yangjeh, M. Abitorabi, A. Rouhi, Magnetically separable nanocomposites based on ZnO and their applications in photocatalytic processes: a review, *Crit. Rev. Environ. Sci. Technol.* 48 (2018) 806–857, <https://doi.org/10.1080/10643389.2018.1487227>.
- [12] X. Chen, Y. Zhou, Q. Liu, Z. Li, J. Liu, Z. Zou, Ultrathin, single-crystal WO₃ nanosheets by two-dimensional oriented attachment toward enhanced photocatalytic reduction of CO₂ into hydrocarbon fuels under visible light, *ACS Appl. Mater. Interfaces* 4 (2012) 3372–3377, <https://doi.org/10.1021/am300661s>.
- [13] J. Jin, J. Yu, D. Guo, C. Cui, W. Ho, A hierarchical Z-scheme CdS-WO₃ photocatalyst with enhanced CO₂ reduction activity, *Small* 11 (2015) 5262–5271, <https://doi.org/10.1002/smll.201500926>.
- [14] Q. Liu, Y. Zhou, J. Kou, X. Chen, Z. Tian, J. Gao, S. Yan, Z. Zou, High-yield synthesis of ultralong and ultrathin Zn₂GeO₄ nanoribbons toward improved photocatalytic reduction of CO₂ into renewable hydrocarbon fuel, *J. Am. Chem. Soc.* 132 (2010) 14385–14387, <https://doi.org/10.1021/ja1068596>.
- [15] S. Cao, B. Shen, T. Tong, J. Fu, J. Yu, 2D/2D heterojunction of ultrathin MXene/Bi₂WO₆ nanosheets for improved photocatalytic CO₂ reduction, *Adv. Funct. Mater.* 28 (2018) 1800136, <https://doi.org/10.1002/adfm.201800136>.
- [16] X. Kong, W. Tan, B.J. Ng, S.P. Chai, A.R. Mohamed, Harnessing Vis-NIR broad spectrum for photocatalytic CO₂ reduction over carbon quantum dots-decorated ultrathin Bi₂WO₆ nanosheets, *Nano Res.* 10 (2017) 1720–1731, <https://doi.org/10.1007/s12274-017-1435-4>.
- [17] P. Li, Y. Zhou, H. Li, Q. Xu, X. Meng, X. Wang, M. Xiao, Z. Zou, All-solid-state Z-scheme system arrays of Fe₂V₄O₁₃/RGO/CdS for visible light-driving photocatalytic CO₂ reduction into renewable hydrocarbon fuel, *Chem. Commun.* 51 (2015) 800–803, <https://doi.org/10.1039/C4CC08744E>.
- [18] Y. Zhao, X. Jia, G.I.N. Waterhouse, L.Z. Wu, C.H. Tung, D. O'Hare, T. Zhang, Layered double hydroxide nanostructured photocatalysts for renewable energy production, *Adv. Energy Mater.* 6 (2016) 1501974, <https://doi.org/10.1002/aenm.201501974>.
- [19] C. Li, M. Wei, D.G. Evans, X. Duan, Recent advances for layered double hydroxides (LDHs) materials as catalysts applied in green aqueous media, *Catal. Today* 247 (2015) 163–169, <https://doi.org/10.1016/j.cattod.2014.05.032>.
- [20] Z. Gu, J.J. Atherton, Z.P. Xu, Hierarchical layered double hydroxide nanocomposites: structure, synthesis and applications, *Chem. Commun.* 51 (2015) 3024–3036, <https://doi.org/10.1039/C4CC0715F>.
- [21] G. Fan, F. Li, D.G. Evans, X. Duan, Catalytic applications of layered double hydroxides: recent advances and perspectives, *Chem. Soc. Rev.* 43 (2014) 7040–7066, <https://doi.org/10.1039/C4CS00160E>.
- [22] N. Ahmed, Y. Shibata, T. Taniguchi, Y. Izumi, Photocatalytic conversion of carbon dioxide into methanol using zinc-copper-M (III)(M = aluminum, gallium) layered double hydroxides, *J. Catal.* 279 (2011) 123–135, <https://doi.org/10.1016/j.jcat.2011.01.004>.
- [23] K. Teramura, S. Iguchi, Y. Mizuno, T. Shishido, T. Tanaka, Photocatalytic conversion of CO₂ in water over layered double hydroxides, *Angew. Chem.* 124 (2012) 8132–8135, <https://doi.org/10.1002/anie.201201847>.
- [24] S. Iguchi, K. Teramura, S. Hosokawa, T. Tanaka, Photocatalytic conversion of CO₂ in water using fluorinated layered double hydroxides as photocatalysts, *Appl. Catal. A Gen.* 521 (2016) 160–167, <https://doi.org/10.1016/j.apcata.2015.11.023>.
- [25] J. Hong, W. Zhang, Y. Wang, T. Zhou, R. Xu, Photocatalytic reduction of carbon dioxide over self-assembled carbon nitride and layered double hydroxide: the role of carbon dioxide enrichment, *ChemCatChem* 6 (2014) 2315–2321, <https://doi.org/10.1002/cctc.201402195>.
- [26] S. Iguchi, Y. Hasegawa, K. Teramura, S. Kidera, S. Kikkawa, S. Hosokawa, H. Asakura, T. Tanaka, Drastic improvement in the photocatalytic activity of Ga₂O₃ modified with Mg-Al layered double hydroxide for the conversion of CO₂ in water, *Sustain. Energ. Fuels* 1 (2017) 1740–1747, <https://doi.org/10.1039/C7SE00204A>.
- [27] S. Kumar, M.A. Isaacs, R. Trofimovaite, C.M.A. Parlett, R.E. Douthwaite, B. Coulson, M.C.R. Cockett, K. Wilson, A.F. Lee, P25@CoAl layered double hydroxide heterojunction nanocomposites for CO₂ photocatalytic reduction, *Appl. Catal. B: Environ.* 209 (2017) 394–404, <https://doi.org/10.1016/j.apcatb.2017.03.006>.
- [28] S. Tonda, S. Kumar, M. Bhardwaj, P. Yadav, S. Ogale, g-C₃N₄/NiAl-LDH 2D/2D hybrid heterojunction for high-performance photocatalytic reduction of CO₂ into renewable fuels, *ACS Appl. Mater. Interfaces* 10 (2018) 2667–2678, <https://doi.org/10.1021/acsmi.7b18835>.
- [29] L. Tang, Z. Zhao, Z. Yong, B. Lv, L. Peng, J. Ye, X. Wang, X. Min, Z. Zou, Series of ZnSn(OH)₆ polyhedra: enhanced CO₂ dissociation activation and crystal facet-based homojunction boosting solar fuel synthesis, *Inorg. Chem.* 56 (2017) 5704–5709, <https://doi.org/10.1021/acs.inorgchem.7b00219>.
- [30] W.J. Ong, L.L. Tan, Y.H. Ng, S.T. Yong, S.P. Chai, Graphitic carbon nitride (g-C₃N₄)-based photocatalysts for artificial photosynthesis and environmental remediation: are we a step closer to achieving sustainability? *Chem. Rev.* 116 (2016) 7159–7329, <https://doi.org/10.1021/acs.chemrev.6b00075>.
- [31] M. Mousavi, A. Habibi-Yangjeh, S.R. Pouran, Review on magnetically separable graphitic carbon nitride-based nanocomposites as promising visible-light-driven photocatalysts, *J. Mater. Sci. Mater. Electron.* 29 (2018) 1719–1747, <https://doi.org/10.1007/s10854-017-8166-x>.
- [32] M.Q. Wen, T. Xiong, Z.G. Zang, W. Wen, T. Tang, F. Dong, Synthesis of MoS₂/g-C₃N₄ nanocomposites with enhanced visible-light photocatalytic activity for the removal of nitric oxide (NO), *Opt. Express* 24 (2016) 10205–10212, <https://doi.org/10.1364/OE.24.010205>.
- [33] M. Mousavi, A. Habibi-Yangjeh, D. Seifzadeh, Novel ternary g-C₃N₄/Fe₃O₄/MnWO₄ nanocomposites: synthesis, characterization, and visible-light photocatalytic performance for environmental purposes, *J. Mater. Sci. Technol.* 34 (2018) 1638–1651, <https://doi.org/10.1016/j.jmst.2018.05.004>.
- [34] Y. Li, Y. Xue, J. Tian, X. Song, X. Zhang, X. Wang, H. Cui, Silver oxide decorated graphitic carbon nitride for the realization of photocatalytic degradation over the full solar spectrum: from UV to NIR region, *Sol. Energy Mater. Sol. Cells* 168 (2017) 100–111, <https://doi.org/10.1016/j.solmat.2017.04.031>.
- [35] M. Mousavi, A. Habibi-Yangjeh, Decoration of Fe₃O₄ and CoWO₄ nanoparticles over graphitic carbon nitride: novel visible-light-responsive photocatalysts with exceptional photocatalytic performances, *Mater. Res. Bull.* 105 (2018) 159–171, <https://doi.org/10.1016/j.materresbull.2018.04.052>.
- [36] Y. Zheng, L. Lin, B. Wang, X. Wang, Graphitic carbon nitride polymers toward sustainable photoredox catalysis, *Angew. Chem. Int. Ed.* 54 (2015) 12868–12884, <https://doi.org/10.1002/anie.201501788>.
- [37] S. Asadzadeh-Khaneghab, A. Habibi-Yangjeh, K. Yubuta, Novel g-C₃N₄ nanosheets/CDs/BiOCl photocatalysts with exceptional activity under visible light, *J. Am. Ceram. Soc.* 102 (2019) 1435–1453, <https://doi.org/10.1111/jace.15959>.
- [38] H. Diarmand-Khalilabad, A. Habibi-Yangjeh, D. Seifzadeh, S. Asadzadeh-Khaneghab, E. Vesali-Kermani, g-C₃N₄ nanosheets decorated with carbon dots and CdS nanoparticles: novel nanocomposites with excellent nitrogen photofixation ability under simulated solar irradiation, *Ceram. Int.* 45 (2019) 2542–2555, <https://doi.org/10.1016/j.ceramint.2018.10.185>.
- [39] M. Mousavi, A. Habibi-Yangjeh, Integration of NiWO₄ and Fe₃O₄ with graphitic carbon nitride to fabricate novel magnetically recoverable visible-light-driven photocatalysts, *J. Mater. Sci.* 53 (2018) 9046–9063, <https://doi.org/10.1007/s10853-018-2213-8>.
- [40] W.S. Hummers Jr, R.E. Offeman, Preparation of graphitic oxide, *J. Am. Chem. Soc.*

80 (1958) 1339, <https://doi.org/10.1021/ja01539a017>.

[41] T.-H. Kim, W.-J. Lee, J.-Y. Lee, S.-M. Paek, J.-M. Oh, Isomorphous substitution of divalent metal ions in layered double hydroxides through a soft chemical hydro-thermal reaction, *Dalton Trans.* 43 (2014) 10430–10437, <https://doi.org/10.1039/c4dt00373j>.

[42] X. Wang, K. Maeda, A. Thomas, K. Takanabe, G. Xin, J.M. Carlsson, K. Domen, Ma. Antonietti, A metal-free polymeric photocatalyst for hydrogen production from water under visible light, *Nat. Mater.* 8 (2009) 76–80, https://doi.org/10.1142/9789814317665_0039.

[43] S. Ziegenhein, G. Varga, M. Szabados, P. Sipos, I. Pálinkó, Cu (II) Cr (III)-LDH: synthesis, characterization, intercalation properties and a catalytic application, *Chem. Pap.* 72 (2018) 897–902, <https://doi.org/10.1007/s11696-017-0352-z>.

[44] L. Mohapatra, D. Patra, K. Parida, S.J. Zaidi, Enhanced photocatalytic activity of a molybdate-intercalated iron-based layered double hydroxide, *Eur. J. Inorg. Chem.* 3 (2017) 723–733, <https://doi.org/10.1002/ejic.201601191>.

[45] M. Dong, J. Wu, M. Gao, Y. Xin, T. Ma, Y. Sun, Fabrication of Z-scheme g-C₃N₄/RGO/Bi₂WO₆ photocatalyst with enhanced visible-light photocatalytic activity, *Chem. Eng. J.* 290 (2016) 136–146, <https://doi.org/10.1016/j.cej.2016.01.031>.

[46] S. Guo, Y. Tang, Y. Xie, C. Tian, Q. Feng, W. Zhou, B. Jiang, P-doped tubular g-C₃N₄ with surface carbon defects: universal synthesis and enhanced visible-light photocatalytic hydrogen production, *Appl. Catal. B Environ.* 218 (2017) 664–671, <https://doi.org/10.1016/j.apcatb.2017.07.022>.

[47] Y. Han, Z.H. Liu, Z. Yang, Z. Wang, X. Tang, T. Wang, Preparation of Ni²⁺–Fe³⁺ layered double hydroxide material with high crystallinity and well-defined hexagonal shapes, *Chem. Mater.* 20 (2008) 360–363, <https://doi.org/10.1021/cm7023789>.

[48] L. El Gaini, M. Lakraimi, E. Sebbar, A. Megheia, M. Bakasse, Removal of indigo carmine dye from water to Mg-Al-CO₃-calcined layered double hydroxides, *J. Hazard. Mater.* 161 (2009) 627–632, <https://doi.org/10.1016/j.jhazmat.2008.04.089>.

[49] C. Zhao, L. Liu, G. Rao, H. Zhao, L. Wang, J. Xu, Y. Li, Synthesis of novel MgAl layered double oxide grafted TiO₂ cuboids and their photocatalytic activity on CO₂ reduction with water vapor, *Catal. Sci. Technol.* 5 (2015) 3288–3295, <https://doi.org/10.1039/C5SCY00216H>.

[50] C. Gu, H. Zhang, X. Wang, J. Tu, Synthesis of reduced graphene oxide by an ionothermal method and electrochemical performance, *RSC Adv.* 3 (2013) 11807–11815, <https://doi.org/10.1039/C3RA41485J>.

[51] M. Ou, W. Tu, S. Yin, W. Xing, S. Wu, H. Wang, S. Wan, Q. Zhong, R. Xu, Amino-assisted anchoring of CsPbBr₃ perovskite quantum dots on porous g-C₃N₄ for enhanced photocatalytic CO₂ reduction, *Angew. Chem. Int. Ed.* 57 (2018) 13570–13574, <https://doi.org/10.1002/ange.201808930>.

[52] Y. Wang, X. Bai, H. Qin, F. Wang, Y. Li, X. Li, S. Kang, Y. Zuo, L. Cui, Facile one-step synthesis of hybrid graphitic carbon nitride and carbon composites as high-performance catalysts for CO₂ photocatalytic conversion, *ACS Appl. Mater. Interface* 8 (2016) 17212–17219, <https://doi.org/10.1021/acsami.6b03472>.

[53] Y. Dou, S. Zhang, T. Pan, S. Xu, A. Zhou, M. Pu, H. Yan, J. Han, M. Wei, D.G. Evans, X. Duan, TiO₂@layered double hydroxide core-shell nanospheres with largely enhanced photocatalytic activity toward O₂ generation, *Adv. Funct. Mater.* 25 (2015) 2243–2249, <https://doi.org/10.1002/adfm.201404496>.

[54] C. Wang, B. Ma, S. Xu, D. Li, S. He, Y. Zhao, J. Han, M. Wei, D.G. Evans, X. Duan, Visible-light-driven overall water splitting with a largely-enhanced efficiency over a Cu₂O/ZnCr-layered double hydroxide photocatalyst, *Nano Energy* 32 (2017) 463–469, <https://doi.org/10.1016/j.nanoen.2017.01.010>.

[55] Y. Pan, Y. Lin, Y. Chen, Y. Liu, C. Liu, Cobalt phosphide-based electrocatalysts: synthesis and phase catalytic activity comparison for hydrogen evolution, *J. Mater. Chem. A* 4 (2016) 4745–4754, <https://doi.org/10.1039/C6TA00575F>.

[56] J. Liu, Y. Liu, N. Liu, Y. Han, X. Zhang, H. Huang, Y. Lifshitz, S.T. Lee, J. Zhong, Z. Kang, Metal-free efficient photocatalyst for stable visible water splitting via a two-electron pathway, *Science* 347 (2015) 970–974, <https://doi.org/10.1126/science.aaa3145>.

[57] X. Xiang, F. Pan, Y. Li, A review on adsorption-enhanced photoreduction of carbon dioxide by nanocomposite materials, *Adv. Compos. Hybrid Mater.* 1 (2018) 6–31, <https://doi.org/10.1007/s42114-017-0001-6>.

[58] L. Lu, B. Wang, S. Wang, Z. Shi, S. Yan, Z. Zou, La₂O₃-modified LaTiO₂N photocatalyst with spatially separated active sites achieving enhanced CO₂ reduction, *Adv. Funct. Mater.* 27 (2017) 1702447, , <https://doi.org/10.1002/adfm.201702447>.

[59] W. Wu, K. Bhattacharyya, K. Gray, E. Weitz, Photoinduced reactions of surface-bound species on titania nanotubes and platinized titania nanotubes: an in Situ FTIR Study, *J. Phys. Chem. C* 117 (2013) 20643–20655, <https://doi.org/10.1021/jp405902a>.

[60] L. Liu, H. Zhao, J. Andino, Y. Li, Photocatalytic CO₂ reduction with H₂O on TiO₂ nanocrystals: comparison of anatase, rutile, and brookite polymorphs and exploration of surface chemistry, *ACS Catal.* 2 (2012) 1817–1828, <https://doi.org/10.1021/cs300273q>.

[61] L. Liu, C. Zhao, Y. Li, Spontaneous dissociation of CO₂ to CO on defective surface of Cu(II)/TiO_{2-x} nanoparticles at room temperature, *J. Phys. Chem. C* 116 (2012) 7904–7912, <https://doi.org/10.1021/jp300932b>.

[62] Y. Wang, J. Zhao, T. Wang, Y. Li, X. Li, J. Yin, C. Wang, CO₂photoreduction with H₂O vapor on highly dispersed CeO₂/TiO₂ catalysts: Surface species and their reactivity, *J. Catal.* 337 (2016) 293–302, <https://doi.org/10.1016/j.jcat.2015.12.030>.

[63] J. Wu, X. Li, W. Shi, P. Ling, Y. Sun, X. Jiao, S. Gao, L. Liang, J. Xu, W. Yan, C. Wang, Y. Xie, Efficient visible-light-driven CO₂ reduction mediated by defect-engineered BiOBr atomic layers, *Angew. Chem. Int. Ed.* 57 (2018) 8719–8723, <https://doi.org/10.1002/ange.201803514>.

[64] L. Liu, W. Fan, X. Zhao, H. Sun, P. Li, L. Sun, Surface dependence of CO₂ adsorption on Zn₂GeO₄, *Langmuir* 28 (2012) 10415–10424, <https://doi.org/10.1021/la301679h>.

[65] H. Li, Y. Gao, Y. Zhou, F. Fan, Q. Han, Q. Xu, X. Wang, M. Xiao, C. Li, Z. Zou, Construction and nanoscale detection of interfacial charge transfer of elegant Z-scheme WO₃/Au/In₂S₃ nanowire arrays, *Nano Lett.* 16 (2016) 5547–5552, <https://doi.org/10.1021/acs.nanolett.6b02094>.

[66] B. Sun, W. Zhou, H. Li, L. Ren, P. Qiao, W. Li, H. Fu, Synthesis of particulate hierarchical tandem heterojunctions toward optimized photocatalytic hydrogen production, *Adv. Mater.* 30 (2018) 1804282, , <https://doi.org/10.1002/adma.201804282>.

[67] J. Bian, Q. Li, C. Huang, J. Li, Y. Guo, M. Zaw, R.Q. Zhang, Thermal vapor condensation of uniform graphitic carbon nitride films with remarkable photocurrent density for photoelectrochemical applications, *Nano Energy* 15 (2015) 353–361, <https://doi.org/10.1016/j.nanoen.2015.04.012>.

[68] Z. Zhang, J.T. Yates, Band bending in semiconductors: chemical and physical consequences at surfaces and interfaces, *Chem. Rev.* 112 (2012) 5520–5551, <https://doi.org/10.1021/cr3000626>.

[69] T. Xiao, Z. Tang, Y. Yang, L. Tang, Y. Zhou, Z. Zou, In situ construction of hierarchical WO₃/g-C₃N₄ composite hollow microspheres as a Z-scheme photocatalyst for the degradation of antibiotics, *Appl. Catal. B Environ.* 220 (2018) 417–428, <https://doi.org/10.1016/j.apcatb.2017.08.070>.

[70] W.H. Wang, Y. Himeda, J.T. Muckerman, G.F. Manbeck, E. Fujita, CO₂ hydrogenation to formate and methanol as an alternative to photo-and electrochemical CO₂ reduction, *Chem. Rev.* 115 (2015) 12936–12973, <https://doi.org/10.1021/acs.chemrev.5b00197>.

[71] S. Jorfi, B. Kakavandi, H.R. Motlagh, M. Ahmadi, N. Jaafarzadeh, A novel combination of oxidative degradation for benzotriazole removal using TiO₂ loaded on Fe^{II}Fe₂^{III}O₄@C as an efficient activator of peroxymonosulfate, *Appl. Catal. B: Environ.* 219 (2017) 216–230, <https://doi.org/10.1016/j.apcatb.2017.07.035>.

[72] P. Xiong, Q. Chen, M. He, X. Sun, X. Wang, Cobalt ferrite-polyaniline hetero-architecture: a magnetically recyclable photocatalyst with highly enhanced performances, *J. Mater. Chem. C* 22 (2012) 17485–17493, <https://doi.org/10.1039/c2jm31522j>.

[73] Z. Jiang, W. Wan, H. Li, S. Yuan, H. Zhao, P.K. Wong, A hierarchical Z-scheme α-Fe₂O₃/g-C₃N₄ hybrid for enhanced photocatalytic CO₂ reduction, *Adv. Mater.* 30 (2018) 1706108, , <https://doi.org/10.1002/adma.201706108>.

[74] C. Chen, W. Ma, J. Zhao, Semiconductor-mediated photodegradation of pollutants under visible-light irradiation, *Chem. Soc. Rev.* 39 (2010) 4206–4219, <https://doi.org/10.1039/B921692H>.

[75] Y. Hong, Y. Jiang, C. Li, W. Fan, X. Yan, M. Yan, W. Shi, In-situ synthesis of direct solid-state Z-scheme V₂O₅/g-C₃N₄ heterojunctions with enhanced visible light efficiency in photocatalytic degradation of pollutants, *Appl. Catal. B: Environ.* 180 (2016) 663–673, <https://doi.org/10.1016/j.apcatb.2015.06.057>.